Chapter 6

The microstructural and mechanical behavior of in-situ synthesized ZrB_2-ZrC and ZrB_2-SiC-ZrC composites

6. 1 Introduction

In the present investigation, the ZrB_2-ZrC and ZrB_2-SiC-ZrC composites were fabricated via an in-situ reduction mechanism using ZrO_2, B_4C, Si, and graphite fine powder at 1900°C in an argon atmosphere. The boro/carbothermal reduction produced nano-sized ZrC grains with ZrB_2 particles at 1600°C, whereas the incorporation of Si content had nano-sized homogeneous distributed SiC grains with ZrB_2-ZrC particles. The temperature increased to 1600°C, and the resulting composite's stable ZrC phase became evident. In the ZrB_2-based composite densification, microstructure, mechanical, and chemical state identification of elements were investigated. The densification in the samples improved with the formation of ZrC and SiC content, correlated with the micrographs and mechanical properties of the samples. The chemical state identification confirms the trace amount of intermediate zirconium oxycarbide in the ZrB_2-based composite. Compared to binary ZrB_2-ZrC composite, ZrB_2-SiC-ZrC composite has finer microstructure and higher densification.

Commercially available starting raw materials were used for the fabrication of ZrB_2-ZrC and ZrB_2-SiC-ZrC composites. The detailed specification of starting materials and their corresponding characteristics is explained in Table 3.1. Table 6.1 presents a detailed description of the composite material prepared using various starting raw materials. The table provides comprehensive information on the raw materials used and their proportions and compositions. The starting powders were ball milled in a planetary mill for 6 h at 230 rpm using a zirconia ball as the grinding body. The powder and zirconia balls ratio was 1:10. The diameter of the samples was 10 mm, with a thickness of 5 mm, compacted at a pressure of 12 MPa. Subsequently, the samples dried at 100°C for 24 hours.

The occurred reactions were the following:

$$ZrO_2\ (s) + 0.5B_4C\ (s) + 1.5C(s) \rightarrow ZrB_2\ (s) + 2CO\ (g) \qquad (6.1)$$

$$ZrO_2\ (s) + 0.5B_4C\ (s) + 0.5Si\ (s) + 2C \rightarrow ZrB_2\ (s) + 0.5SiC\ (s) + 2CO\ (g) \qquad (6.2)$$

Table 6. 1 The starting powders utilized to fabricate ZrB_2-ZrC and ZrB_2-SiC-ZrC include ZrO_2, B_4C, Si, and graphite, with their respective composition.

Specimen name	Mole content				Calculated (wt %)		
	ZrO_2	B_4C	Graphite	Si	ZrB_2	ZrC	SiC
ZZ	1	0.5	1.5	-	100	-	-
ZSZ	1	0.5	2	0.5	91.85	-	8.15

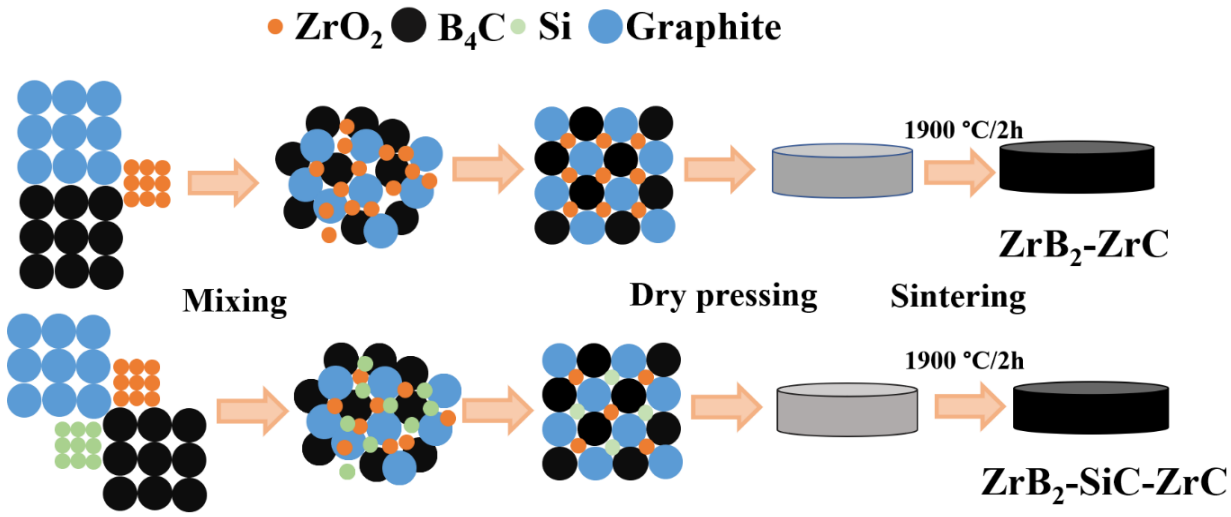

Fig. 6.1 Systematic illustration of fabricated ZrB_2-ZrC and ZrB_2-SiC-ZrC composite via in situ reduction method

The samples were positioned in a vacuum and debinding furnace, maintaining a 10^{-1} millibar vacuum. The composite was heat treated initially at 1600°C with 5°C/ min, held for 1 hr in argon purging, and then sintered at 1900°C at 10°C/min. Table 6.2 mentions the sintering process details for the samples.

Table 6.2. The final product of the heat-treated samples at different temperatures

No:	Sintering stages	Final product

	Stage 1		Stage 2		Stage 3		
	Temperature (°C)	Holding (min)	Temperature (°C)	Holding (min)	Temperature (°C)	Holding (min)	
1	900	30	1300	120	-	-	ZrO_2, B_4C, C
2	900	30	1300	120	-	-	ZrB_2, ZrO_2, B_4C
3	900	30	1400	120	-	-	ZrB_2, B_4C, ZrO_2
4	900	30	1400	120	-	-	ZrB_2, SiC, ZrO_2
5	900	30	1500	120	-	-	ZrB_2, ZrO_2, C
6	900	30	1500	120	-	-	ZrB_2, SiC, ZrO_2
7	900	30	1600	120	-	-	ZrB_2, ZrC
8	900	30	1600	120	-	-	ZrB_2, SiC, ZrC
9	900	30	1600	60	1900	120	ZrB_2, ZrC
10	900	30	1600	60	1900	120	ZrB_2, SiC, ZrC

X-ray diffractometer techniques determined the phase present in synthesized and sintered samples. The Rietveld analysis finds the particular number of phases in the final specimen. Archimedes' principle using distilled water is employed to control the bulk density of the ZZ and ZSZ composite after sintering. The rule of the mixture of compositions determined the theoretical density of the sintered sample. The mechanical properties, such as hardness, flexural strength, and fracture toughness of the ZZ and ZSZ composite, were determined, as mentioned in Chapter 3.

6. 2 Result and discussion

6.2.1 Thermodynamic calculation

The equations' change in Gibbs phase energy (ΔG°) provides information about its feasibility at elevated temperatures. The ΔG° for Reaction (6.1) and Reaction (6.2) at different temperatures were calculated using FACTSage thermochemical software [176]. The possible feasible Reaction (6.1) temperature is 1418°C under standard conditions ($P=1.013*10^5$ Pa). Similarly, the feasibility of Reaction (6.2) is confirmed at 1324 °C, which is lower than

Reaction (6.1). The ΔG° of Reaction (6.1) and Reaction (6.2) is negative at 1418°C and 1324 °C, respectively, and it reduces with increasing the formation temperature. Some of ZrO_2 initially reacts with B_4C, and an intermediate B_2O_3 phase is formed. This intermediate B_2O_3 phase is further combined with residual ZrO_2, and ZrB_2 is produced. The Reaction (6.2) can be feasible at room temperature and above 28°C in a self-sufficient manner, accordingly to thermodynamic calculations. This Reaction is inadequate to survive independently without meeting the Merzhanov requirement since it is a self-propagating high-temperature (SHS) [4]. But ZrO_2 cannot react with B_4C at room temperature, requiring the maximum temperature for attaining the given Reaction. At the same time, some of the ZrO_2 was reduced with graphite by the carbothermal reduction mechanism, and ZrC formed with CO synthesis and sintering of ZrB_2-based composite.

The synthesis mechanism of ZrB_2-ZrC at different temperature ranges of 1300-1600°C in Fig 6.2. The X-ray diffraction (XRD) analysis of the ZrB_2-ZrC ceramic composite consisted of a high amount of unreacted ZrO_2, B_4C, and graphite at 1300°C and a small amount of ZrB_2 phase. The detection of ZrB_2 occurs at 1300°C and above only via boro carbo thermal reduction of ZrO_2 with B_4C and graphite. At 1400°C, the intense peak of ZrB_2 with a minor amount of residual ZrO_2 and B_4C. However, at 1500°C, a significant amount of ZrB_2 peak is seen with residual ZrO_2 until the 1500°C ZrC formation has not occurred. Therefore, a high temperature is required for ZrC development by reducing ZrO_2.

Further increasing the temperature of the ZrB_2-ZrC sample up to 1600°C, the ZrB_2 and ZrC phases have been observed without residual ZrO_2 and other impurities. The ZrB_2-ZrC composite has occurred at 1600°C. The high vacuum pressure and argon supply lowered the saturation temperature. Another crucial factor to consider is that the argon environment prevented the vaporization of B_2O_3, which meant no more B_4C needs for the ZrO_2 reduction to

create the ZrB_2-based composite. Thus, the results concluded that ZrO_2, B_4C, and graphite converted into the ZrB_2-ZrC phase.

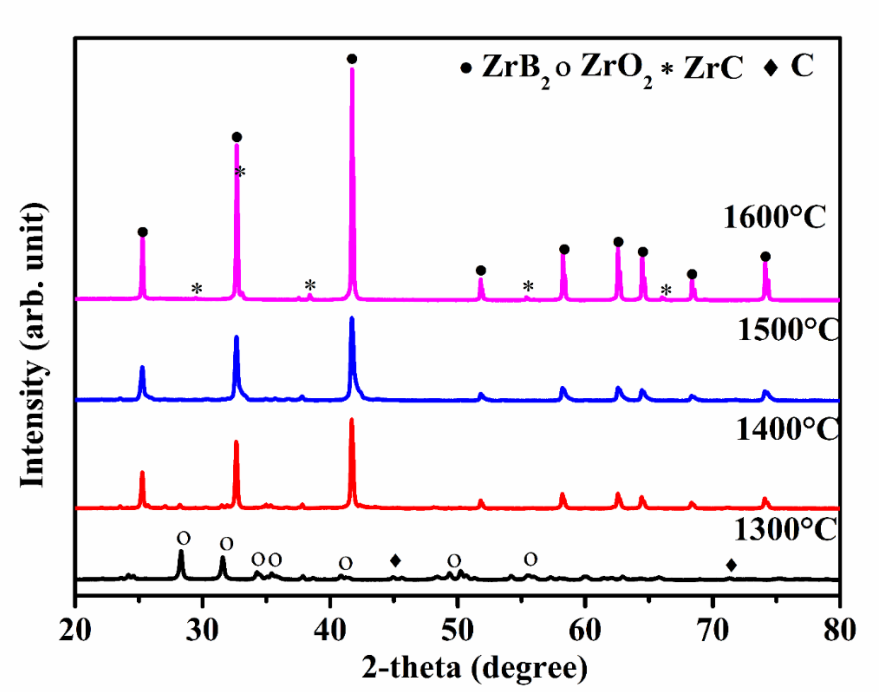

Fig. 6.2 X-ray diffraction pattern of ZZ samples processed at temperatures ranging from 1300°C to 1600°C

The XRD analysis of the ZrB_2-SiC-ZrC composite at a temperature range of 1300-1600°C is shown in Fig 6.3. At 1300°C, ZrO_2, B_4C, and graphite are present with a small amount of ZrB_2 and SiC phase. The formation of the SiC phase occurs at 1300 °C. The ZrC was not detected at 1300°C due to the instability of ZrC in the occurrence of B_4C and Si. Furthermore, the temperature increased 1400°C-1500 °C, and the intensity of the ZrB_2 and SiC phases slightly improved with a minimum amount of ZrO_2 and graphite in the powders. Further increasing the temperature of the ZrB_2-SiC-ZrC sample up to 1600°C, the ZrB_2, SiC, and ZrC phases have been observed without residual ZrO2 and other impurities. At 1600°C, the complete formation of ZrO_2, B_4C, Si, and graphite has occurred in the ZrB_2-SiC-ZrC phase.

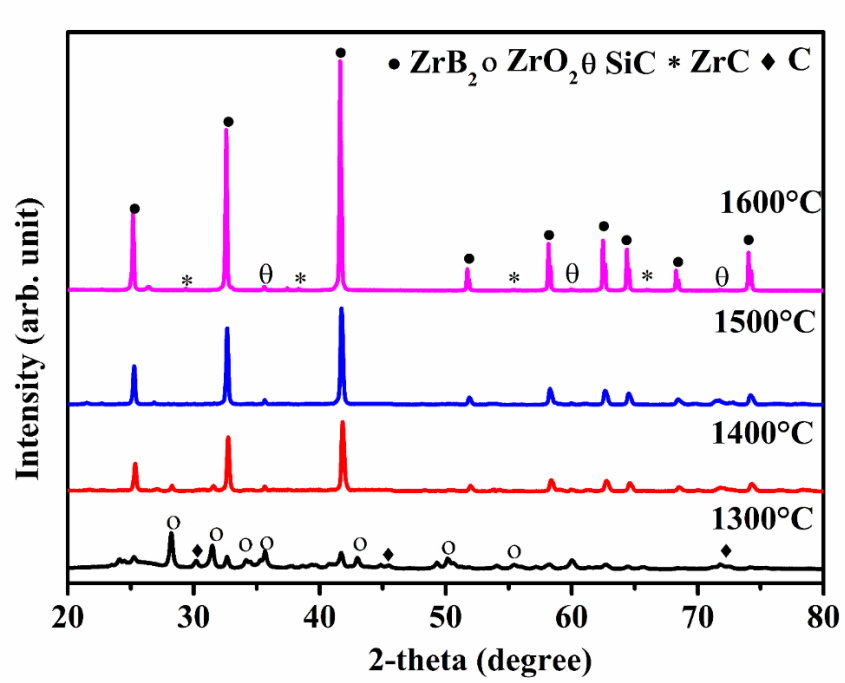

Fig. 6.3 X-ray diffraction pattern of ZSZ samples processed at temperatures ranging from 1300°C to 1600°C

The XRD pattern of ZrB_2-ZrC (ZZ) and ZrB_2-SiC-ZrC (ZSZ) composites sintered at 1900°C, as illustrated in Fig 6.4. The Reaction (6.1) is not satisfied at high temperatures due to intermediate formation and vaporization loss of the B_2O_3 product. The trace amount of ZrO_2 reacts with the carbon of B_4C and graphite, producing a considerable amount of ZrC at a higher temperature. The Rietveld refinement analysis determines the amount of phase in the ZrB_2-based composite. In the ZZ-based composite, the wt % of ZrB_2 and ZrC is 95.2 % and 4.8 %, respectively.

Similarly, the complete formation of ZrB_2 and SiC has not occurred by reaction (6.2) due to the vaporization loss of intermediate B_2O_3 product and residual ZrO_2 reacting with graphite and producing a considerable amount of ZrC. For ZSZ-based composite, the wt % of ZrB_2, SiC, and ZrC is 89.6 %, 8.2 %, and 2.2 %, respectively. The amount of SiC is less than the calculated value due to the formation of CO in the form of a gaseous state. The vaporized

CO may create porosity during 1300-1500°C, but at 1900°C, the ZrB_2-based composite has more kinetic energy, thus allowing them to move closer together and enhance densification.

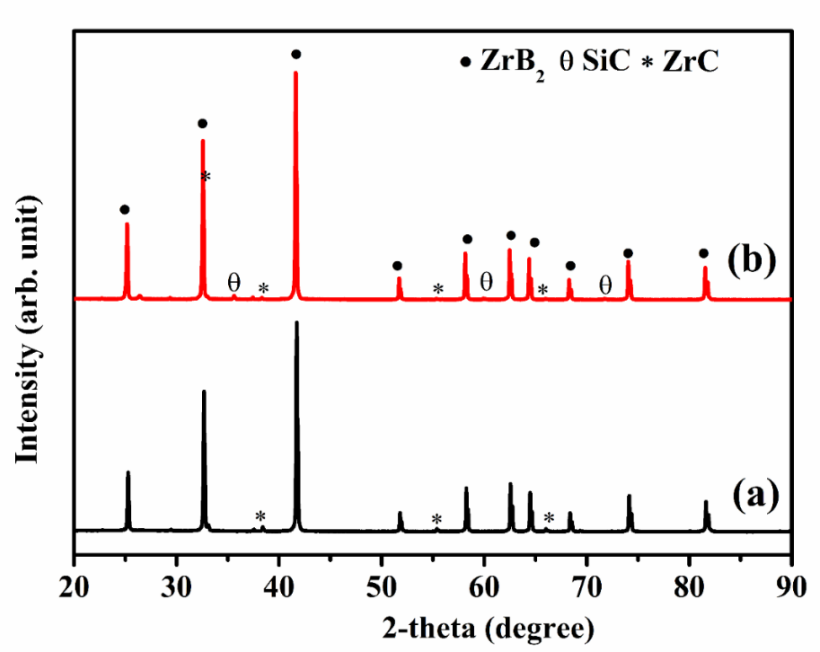

Fig. 6.4 XRD pattern of (a) ZrB_2-ZrC (b) ZrB_2-SiC-ZrC sintered at 1900°C

The transmission electron image of the ZrB_2-ZrC-based composite is demonstrated in Fig. 6.5 (a). The TEM image revealed that the 100 nm nanoparticle is covered with an amorphous phase approximately 4.5 nm thick. Fig. 6.5 (b) shows the HRTEM of the around-rounded particle. The inner lattice image of Fig. 6.5. (b) shows the interplanar distance of 0.352 nm, corresponding to the most preferred (001) orientation of ZrB_2.

Fig. 6.5 (c)-(d) illustrate the TEM analysis of ZrB_2-SiC-ZrC-based composites. Fig 6.5 (c) displays that the grain size of the composites varies within the range of 400-500 nm. Meanwhile, Fig. 6.5 (d) depicts the pattern of selected electron area diffraction (SEAD) of Fig. 6.6 (c). This pattern includes crystal planes of ZrB_2, specifically (001), (100), and (101) along the [010] zone axis.

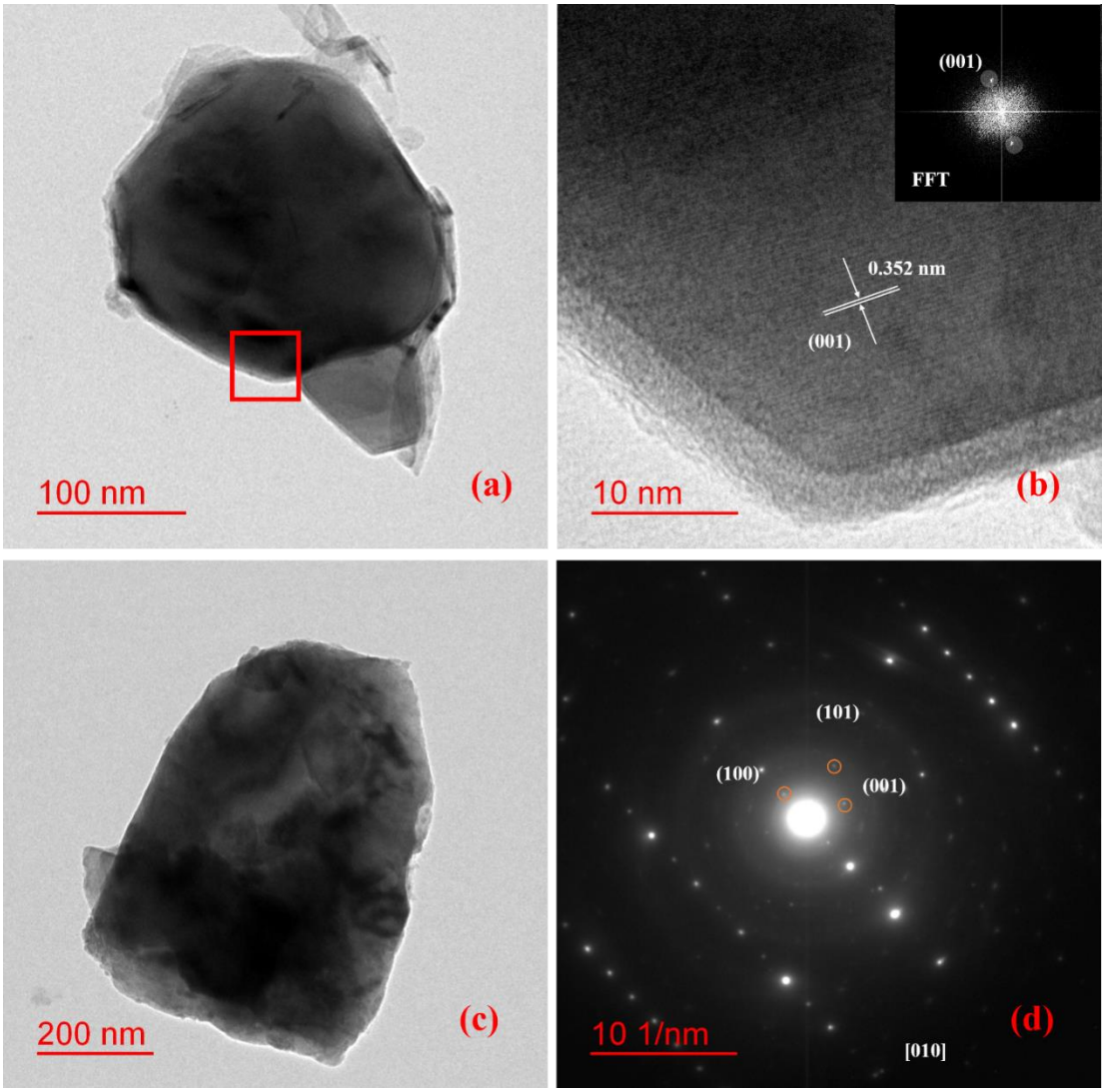

Fig. 6.5 TEM image of (a) ZrB_2-based composite (b) HRTEM of (a)(c) ZrB_2-SiC-ZrC-based composites (d) SEAD pattern of (c)

6.2.2 XPS analysis

X-ray photoelectron spectroscope identifies the chemical compositions, chemical bonding, and oxidation state between the elements present in the ZZ and ZSZ samples. The binding energy was charge-referenced using internal BE (binding energy) referenced [183,188]. Fig. 6.6 shows the survey spectrum of ZZ (ZrB_2-ZrC) and ZSZ (ZrB_2-SiC-ZrC) samples. The sample ZZ comprises significant components of the spectrum B1s, Zr 3d, C1s, and O 1s, and minor spectrum components are little peaks of Zr 3s, Zr $3p_{1/2}$ Zr $3p_{3/2}$, Zr 4s, and O 2s. Similarly, the sample ZSZ comprises significant components of the spectrum B 1s, Zr

3d, Si 2p, C 1s, and O 1s. The minor spectrum of minor peaks of Zr 3s, Zr $3p_{1/2,}$ Zr $3p_{3/2}$, Si 2s, Zr 4s. The binding energy and chemical bonds present in the sintered sample are shown in Table 6.3.

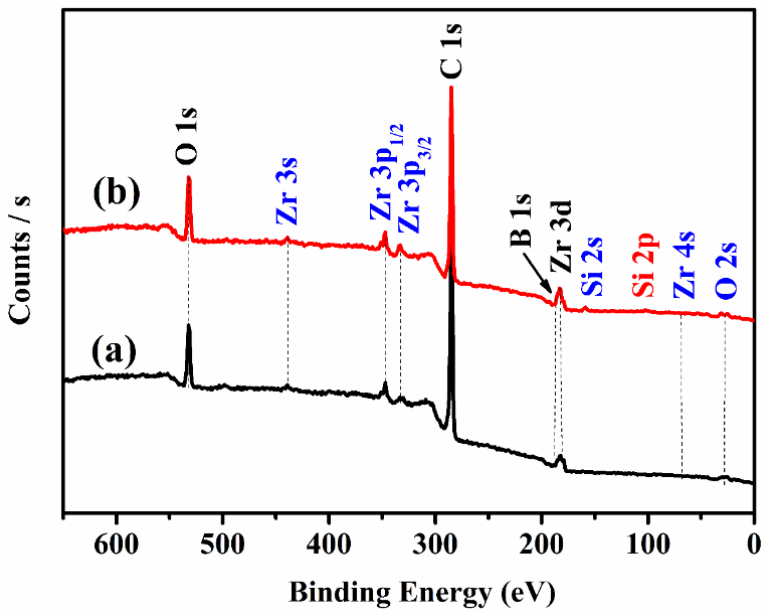

Fig. 6.6 XPS survey of ZrB_2-based composite sintered at 1900°C (a) ZZ (b) ZSZ

The oxygen binding energy of the sample ZZ and ZSZ were illustrated in Fig 6.7 (a)-6.7 (b). In the ZZ and ZSZ samples, the binding energy signal of O 1s is centered at 531. ± 0.1 eV and 531.48± 0.1 eV, respectively, due to the formation of a small amount of ZrO_2 layer and intermediate zirconium oxycarbide (ZrO_xC_y)[186,208]. The XPS spectra of oxygen are fitted into two components. Absorbed oxygen O_{Ads} are attributed to chemically absorbed oxygen on the surface through atmospheric contamination. It is commonly known as $ZrB_{2,}$ and ZrC is very susceptible to the formation of ZrO_2 and ZrO_xC_y due to oxidation of the surface in the presence of atmospheric oxygen. The XRD analysis could not detect the surface formation of ZrO_2.

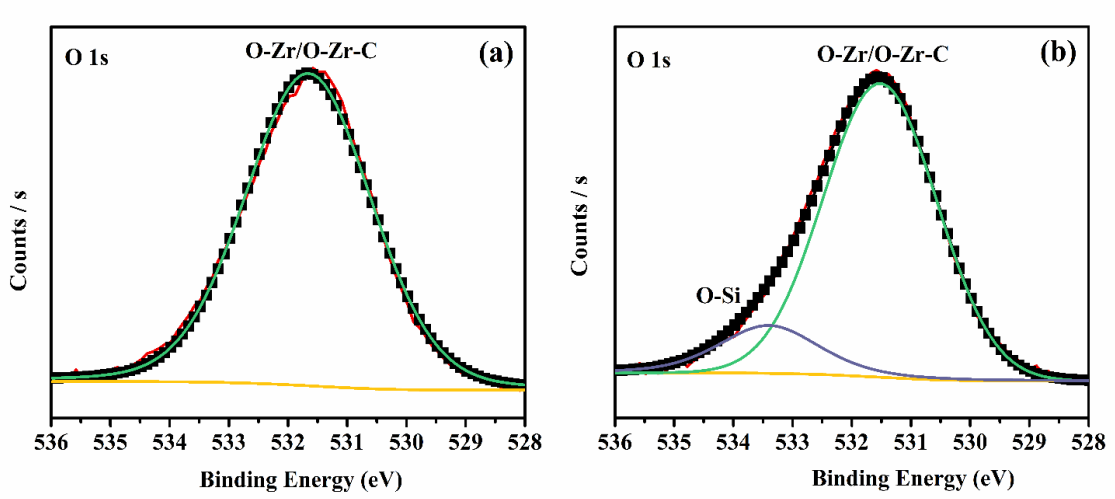

Fig. 6.7 Oxygen binding energy of ZrB_2-based composite at 1900°C (a) ZZ (b) ZSZ

Figs 6.8 (a) and 6.8 (b) illustrate the existence of B 1s and Z 3d spectrums in ZZ and ZSZ samples, respectively. The B 1s peak of ZZ and ZSZ samples were present at 187.8± 0.1 eV and 187.8± 0.1 eV, respectively, connected with the B-Zr bond in the ZrB_2 compound [184]. However, the Z 3d spectrum fits into four peaks. The spin-orbit energy difference of Zr $3d_{5/2}$ and Zr $3d_{3/2}$ was 2.3± 0.1 eV. The binding energy at 182.5 ± 0.1 eV and 182.5 ± 0.1 eV is linked with Zr $3d_{5/2}$ and Zr $3d_{3/2}$ peak related to Zr-B bonds [184,185].

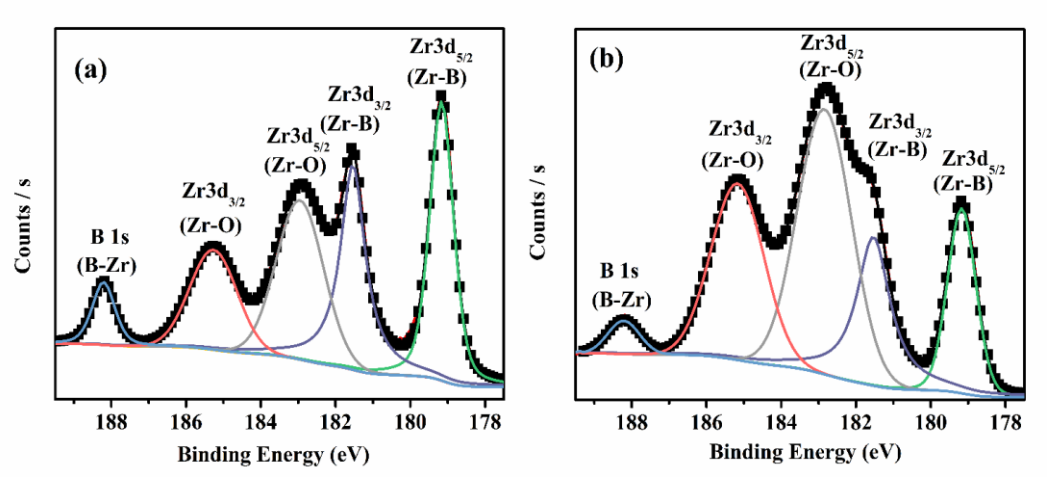

Fig. 6.8 Zr 3d and B 1s binding energy of ZrB_2-based composite at 1900°C (a) ZZ (b) ZSZ

Fig 6.9 (a) and Fig 6.9 (b) demonstrate the C 1s spectra present in the ZZ and ZSZ samples, respectively. The C 1s spectrums of ZZ are fitted into four components. In Fig 6.9 (a), the fitted

with binding energies at 283.2, 284.4, and 285.2 can be referred to as C-Zr, C-C, and C-O, respectively. Similarly, the C 1s spectrums of ZSZ are fitted into five components. In Fig 6.9 (b), the fitted with binding energies at 282.8, 283.3, 284.4, 285.1, and 285.9 can be referred to as C-Si, C-Zr, C-C, C-O, and C=O bonds, respectively. The C-Si, C-Zr, and C-C bonds exist due to the surface's presence of SiC, ZrC, and carbon. Also, the C-O and C=O bonds are associated with oxygen adsorption [208–211].

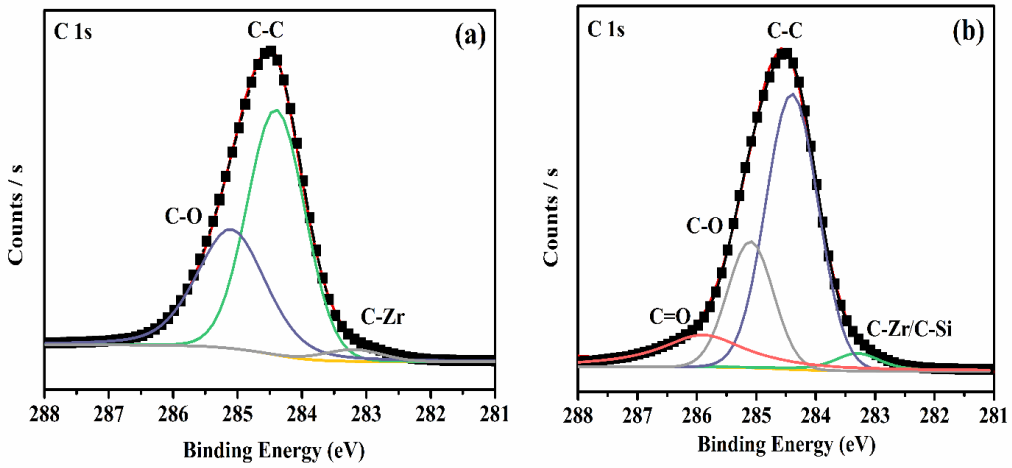

Fig. 6.9 C1s binding energy of ZrB_2-based composite at 1900°C (a) ZZ (b) ZSZ

Table 6.3 XPS spectra of sintered ZrB_2-ZrC (ZZ) and ZrB_2-SiC-ZrC (ZSZ) composite

Elements peak	Binding energy (± 0.1) eV (ZZ)	Binding energy (± 0.1) eV (ZSZ)	Chemical Bond
B 1s	188.2	188.2	B-Zr
Zr 3d 3/2	185.2	185.1	Zr-O
Zr 3d 5/2	182.9	182.8	Zr-O
Zr 3d 3/2	181.5	181.5	Zr-B
Zr 3d 5/2	179.1	179.1	Zr-B
O 1s	531.4	531.5	O-Zr/O-Zr-C
O 1s	-	533.1	O- Si

C 1s	283.2	283.3	C-Zr/ C-Si
C 1s (sp^3)	284.4	284.4	C-C
C 1s	285.2	285.1	C-O
C 1s	-	285.9	C=O

The XRD and XPS analysis results conclude the presence of ZrC and SiC phases in the ZrB_2-based composite. More specifically, the XPS analysis confirms the trace existence of intermediate ZrO_xC_y with ZrC and SiC phases due to active surface oxidation and carburization of the materials under the provided situation.

6.2.3 Density and Microstructural Evaluation

The mixture rule determined the theoretical density of the ZZ and ZSZ. The theoretical density of the ZZ and ZSZ was 6.11 g/cm^3 and 5.85 g/cm^3 when the theoretical density of ZrB_2, SiC, and ZrC was 6.08 g/cm^3, 3.21 g/cm^3, and 6.73 g/cm^3 respectively. The theoretical relative density of the ZZ and ZSZ composite was 90.5% and 92.8%, respectively. The actual wt % of ZrB_2, SiC, and ZrC was taken (Rietveld analysis) instead of the calculated value from reactions (1) and (2). The density of the ZSZ composite is higher than that of the ZZ composite due to the inhabitation of the grain growth of ZrB_2 particles. The in-situ form SiC and ZrC thought that reducing ZrO_2 and Si by graphite (reducing agent) could improve the relative density of the composite. The in situ formed ZrC provides great sinterability and consolidation to composite via decreasing the energy level. However, fine graphite particles act as a lubricant and promote the compaction of particles through the proper rearrangement during dry pressing. Subsequently, it acts as a sintering additive for ZZ and ZSZ composite by eliminating oxide impurities such as ZrO_2, SiO_2, and B_2O_3 by interfacial reaction. Excessive graphite can create porosity and act as a sintering barrier [212].

Figs. 6.10 and 6.11 show the microstructure and morphology of the polished surface of ZZ and ZSZ samples, respectively. In Fig. 6.10 (a), the sample ZZ consists of a trance number of pores with two phases. The nano-sized tiny particles in the grayish phase (spot 1) are homogeneously distributed intergranularly in the bright grayish phase (spot 2), providing densification in the composite. The EDS analysis of spot 1 and spot 2 is illustrated in Fig. 6.10 (b) and Fig. 6.10 (c), respectively. According to the EDS analysis, the dark grayish phase (spot 1) mainly consists of the Zr and C elements, probably related to the ZrC phase. The bright grayish phase (spot 2) primarily consists of Zr, B, and a slight quantity of C.

Similarly, Fig. 6.11 (a) revealed the microstructure and morphology of polished ZSZ samples at 1900°C. Many tiny particles in the dark grayish phase (spot 3) are distributed intergranularly in the light grayish phase (spot 4). The pore size is reduced along with the increase of numerous tiny particles, which enhances the densification of the sample. The dark grayish phase consists of two types of grain within the light grain microstructure, identified through EDS analysis illustrated in Fig. 6.11 (b) and Fig. 6.11 (c). The dark grayish phase was mainly Si, Zr, and C elements, and the light grayish was mainly the Zr and B elements, along with a minor amount of Si and C. The micrograph revealed a slight accumulation of the nano-sized SiC with ZrB_2-ZrC particles. The introduction of Si powder during the fabrication of the ZSZ sample improved the uniformity of SiC particles within the tiny dark grayish phase, which may lead to improved mechanical properties. The ZSZ composite has a finer structure than the ZZ binary-based composite. In multiphase ceramic composition, one ceramic phase is surrounded by another, contributing to mutual tropological relation to interphase boundaries. Therefore, the grain growth of different ceramics phases was simultaneously at a suitable rate and parameters called coupled grain growth.

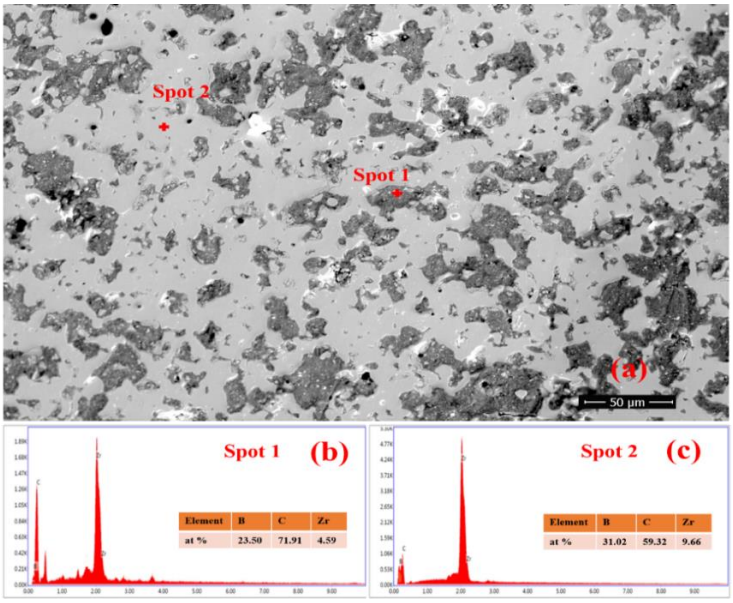

Fig. 6.10 (a). FE-SEM and (b)- (c) EDS of the *polished surface of* ZZ at 1900°C

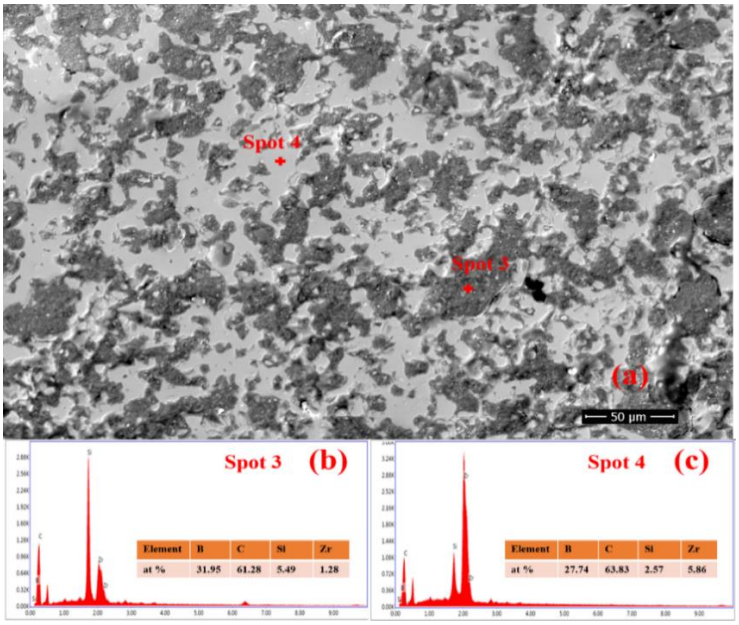

Fig. 6.11 (a) FE-SEM and (b)- (c) EDS of the *polished surface of* ZSZ at 1900°C

6.2.4 Mechanical behavior

The hardness and flexural strength of composites based on ZrB_2-ZrC and ZrB_2-SiC-ZrC were estimated using ZrC and SiC additives shown in Fig. 6.12. The indentation result revealed that the hardness of ZZ and ZSZ samples is 14.2±0.23 GPa and 15.3± 0.3 GPa, respectively. The hardness can be related to the relative density and porosity of the composite.

The pores in the ZZ and ZSZ samples have no resistivity against applied stress by the indenter. The increasing porosity in the ZZ composite may be due to the formation of a higher amount of B_2O_3 gasses during sintering at higher temperatures. The ZZ sample consists of ZrB_2 and ZrC phases along with the trace existence of the intermediate ZrO_xC_y phase. The ZSZ sample also includes the ZrO_xC_y phase. The formation of SiC particles in the composite can slightly increase the hardness of the ZSZ sample. Lin et al. [117] have reported the role of SiC and ZrC addition in ZrB_2-based ceramic. The ZrC and SiC grains are interconnected with significant phase ZrB_2 at 3-4 grain junctions, which restrict each other's grain growth. This demonstrates that the simultaneous addition of ZrC and SiC was beneficial for obtaining the homogenous and finer microstructure of ZrB_2-based ceramics.

Similarly, the flexural strength of the irrespective samples is 219± 0.6 MPa and 196± 0.23 MPa, respectively. The presence of SiC and ZrC particles improves the hardness of ZrB_2-based ceramic and positively impacts the flexural strength. Both samples have slightly high flexural strength with low theoretical density and porosity, which may be due to minimum porosity that can act as crack stoppers, preventing the propagation of cracks during the fracture of the sample [130]. The flexural strength is slightly less in the ZSZ composite due to the formation of the cluster in the sample. Furthermore, the decrease in flexural strength in the ZSZ sample may be due to three-phase ceramic exhibiting more grain boundaries, so the diffusion path is more complex than two-phase ceramic (ZZ) [117].

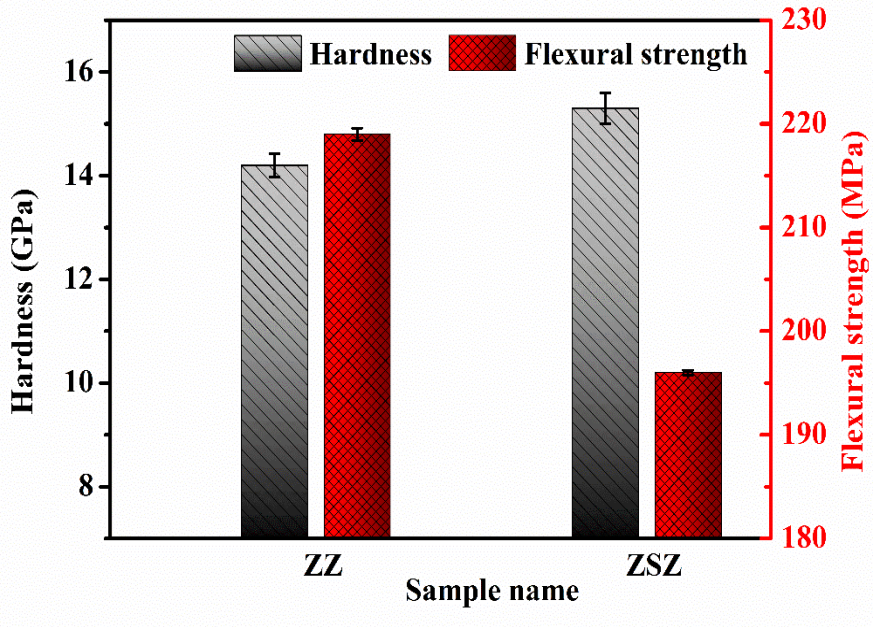

Fig. 6.12 Flexural strength and Vickers hardness of ZrB_2-based composite sintered at 1900°C

The direct crack indentation method was used to calculate the fracture toughness of the composites. The toughening phenomenon of the ZSZ samples was related to the ZrC and SiC content. In this study, due to the significant amounts of porosities presented in the polished surfaces of porous ceramics, the indentation-induced cracks are not observable in all samples. Hence, due to interactions between the pores and cracks in the porous samples, the indentation method is unreliable for the fracture toughness evaluation. Therefore, ANOVA estimations and predictions are meaningless in this case. Thus, the indentation technique was employed only for the ZSZ sintered samples at optimal conditions, and the calculated fracture toughness for the ZSZ samples is 6.1±0.4 MPa $m^{1/2,}$ respectively. The apparent open porosity is approximately 7.1 vol % for ZSZ samples. The SEM micrograph of the crack propagating path for the ZSZ is presented in Fig. 6.13 (a) and Fig. 6.13 (b). Fig. 6.13 (b) are the high-magnification graphs of the crack propagating path for the ZSZ. The SEM image illustrates the in-situ formation of ZrC and SiC particles at ZrB_2 grains. The fracture modes of ZSZ samples are transgranular and intergranular. Due to a lot of porosity in the sample's polished surface, the indentation-induced cracks are not observable. The in-situ formed small SiC and

ZrC grains, restricted the cracks' propagation by the deflection, and boosted the fracture toughness of ZSZ samples by consumption of more fracture energy. The uniform distribution of small SiC and ZrC can enhance the densification and fracture toughness by eliminating the crack tip. Some pores are visible in the micrograph, functioning as crack arrestors during crack propagation.

The fracture toughness is mainly affected by two agents: the grain size of the secondary phase and the open porosity percentage. The formation of SiC and ZrC particles in the composite can increase the fracture toughness of the composite. Open porosity is the second affecting agent on fracture toughness and acts as crack arresting or trapping, which is well-known as another toughening factor. In comparison, its contribution is rather beneficial (5–10%). Under the conditions that the microstructure has no grain refinement and enough densification, more open porosity (more than 10%) not only improves the fracture toughness but also makes it decrease [130]. The additives' type, quantity, and distribution are additional influencing factors, along with secondary grain size and open porosity. The phase diagram of the Zr–B–C system indicates that the solubility limit for ZrC in ZrB_2 is 4.5 wt% [213]. Therefore, incorporating carbon into the ZrB_2 crystal lattice, leading to the formation of an interstitial solid solution, can be considered a third factor contributing to improved fracture toughness. The development of a solid solution is known as a strengthening mechanism for the composite. In this context, it is hypothesized that such a phenomenon enhances grain resistance against the propagation of cracks, ultimately resulting in improved fracture toughness [130].

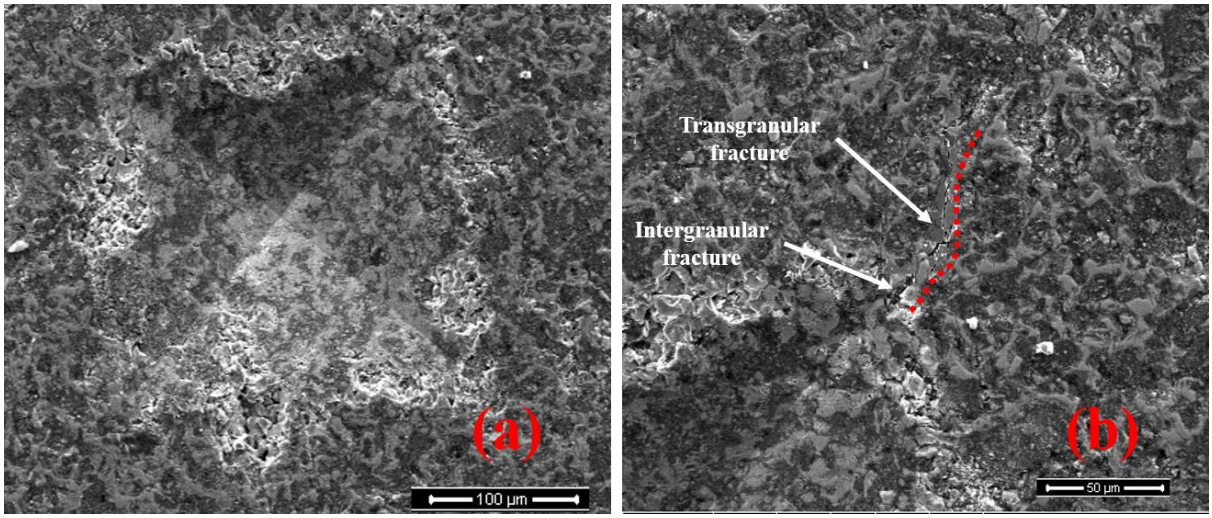

Fig. 6.13 HR-SEM of indentation surface of ZSZ sample sintered at 1900°C (b) crack propagation length of ZSZ

The average grain size of ZrB_2 and (Zr, Si) C for both samples was determined using the linear intercept technique in ImageJ software, as illustrated in Fig. 6.14. The ZrB_2 grains in the ZZ sample exhibited an average size of approximately 10 ± 0.6 µm, while the corresponding ZrC grains measured 21 ± 0.6 nm. Similarly, the ZSZ composite displayed an average grain size of around 8 ± 0.6 µm for ZrB_2 and 28 ± 0.6 nm for (Zr, Si) C. Notably, tiny SiC particles in the composite serve as a grain growth inhibitor, contributing to the reduction of grain coarsening.

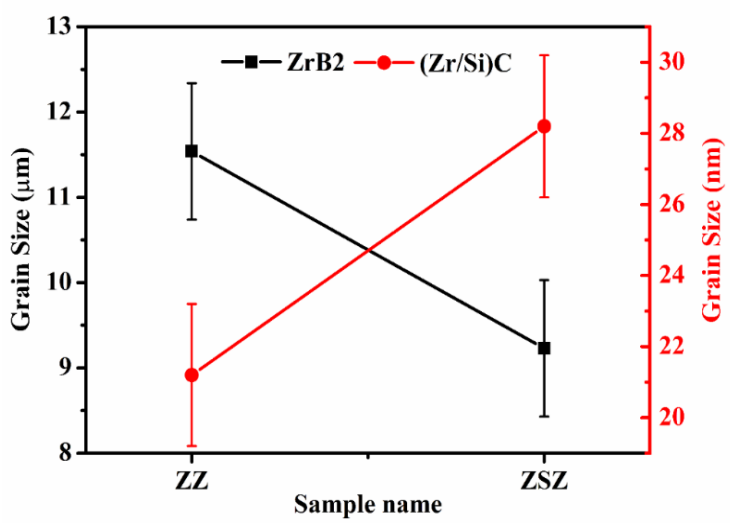

Fig. 6.14 Average grain size of ZrB2 and (Zr/Si) C for ZrB2-based composite sintered at 1900°C

6. 3 Conclusion of the chapter

In our current work, the ZrB_2-ZrC and ZrB_2-SiC-ZrC composite were fabricated at and sintered via in situ boro/carbothermal reduction mechanism using ZrO_2, B_4C, Si, and graphite fine powder (C). B_4C and graphite fine powder are reducing ZrO_2 as a reducing agent. The XPS analysis is applied for the chemical state identification of elements. The chemical state identification confirms the trace amount of intermediate non-stochiometric ZrO_xC_y in the ZrB_2-based composite. Microstructural investigation revealed the in-situ formed ZrC grains distributed in the ZrB_2 particle, whereas the incorporation of Si content produced nano-sized SiC grains with ZrB_2-ZrC particle. The fine particles of ZrC and SiC hindered the grain coarsening during fabrication and sintering at higher temperatures. The relative density of the ZrB_2-ZrC composite was 90.5%, and that of the ZrB_2-SiC-ZrC composite was 92.8%. The mechanical properties were boosted by adding ZrC and SiC content in ZrB_2 composites. Flexural strength was 219± 0.6 MPa and 196± 0.23 MPa, and hardness was increased from 14.2 GPa to 15.3 GPa for ZrB_2-ZrC and ZrB_2-SiC-ZrC composite, respectively. The fracture toughness of ZrB_2-SiC-ZrC was 6.1±0.4 MPa $m^{1/2}$. The thermodynamic calculation investigated the feasibility of reactions at various synthesis temperatures.